THE JOURNAL OF PHYSICAL CHEMISTRY C

Article

pubs.acs.org/JPCC

From $CsPbBr_3$ Nano-Inks to Sintered $CsPbBr_3$–$CsPb_2Br_5$ Films via Thermal Annealing: Implications on Optoelectronic Properties

Francisco Palazon,[†] Sedat Dogan,[†] Sergio Marras,[‡] Federico Locardi,[§] Ilaria Nelli,[§,†] Prachi Rastogi,[†,§] Maurizio Ferretti,[§] Mirko Prato,[‡] Roman Krahne,[†] and Liberato Manna*[,†]

[†]Nanochemistry Department and [‡]Materials Characterization Facility, Istituto Italiano di Tecnologia, Via Morego 30, 16163 Genova, Italy

[§]Dipartimento di Chimica e Chimica Industriale, Università degli Studi di Genova, Via Dodecaneso 31, 16146 Genova, Italy

Supporting Information

ABSTRACT: $CsPbBr_3$ nanocrystals passivated with short molecular ligands and deposited on a substrate were annealed from room temperature to 400 °C in inert atmosphere. Chemical, structural, and morphological transformations were monitored *in situ* and *ex situ* by different techniques, while optoelectronic properties of the film were also assessed. Annealing at 100 °C resulted in a 1 order of magnitude increase in photocurrent and photoresponse as a result of partial sintering of the NCs and residual solvent evaporation. Beyond 150 °C the original orthorhombic NCs were partially transformed into tetragonal $CsPb_2Br_5$ crystals, due to the desorption of weakly bound propionic acid ligands. The photocurrent increased moderately until 300 °C although the photoresponse became slower as a result of the formation of surface trap states. Eventually, annealing beyond 350 °C removed the strongly bound butylamine ligands and reversed the transition to the original orthorhombic phase, with a loss of photocurrent due to the numerous defects induced by the stripping of the passivating butylamine.

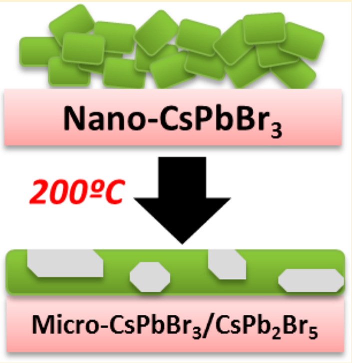

INTRODUCTION

Fully inorganic halide perovskite materials have demonstrated their great potential for implementation in many optoelectronic thin-film devices such as solar cells,[1] light-emitting devices,[2] and photodetectors.[3] Recently, there has been a growing interest in the use of inorganic halide perovskite nanocrystals (NCs) which can be prepared by common colloidal syntheses and used as "inks" for the fabrication of such devices.[4−7] In these cases, the active layer is not formed by a continuous thin film but is rather a mosaic of individual NCs. This methodology usually implies that a considerable amount of organic material (coming from the capping molecular ligands necessary to synthesize the NCs) is also present in the film. In a previous paper,[8] we have shown that thermal annealing of a film of drop-cast $CsPbBr_3$ NCs capped with standard long molecular ligands (oleylamine and oleic acid) resulted in partial sintering of the NCs yielding higher photocurrent and faster photoresponse. We also evidenced a marginal conversion to tetragonal $CsPb_2Br_5$ phase at the highest tested temperature of 200 °C, as confirmed by others,[9] which was not investigated in detail. $CsPb_2Br_5$ NCs obtained by colloidal syntheses have recently been reported.[10−13] The optoelectronic properties of this material, and especially the beneficial or detrimental role that it may play in dual-phase films with $CsPbBr_3$, is an active matter of debate. Indeed, while some groups have claimed high photoluminescence quantum yields up to 87%,[11] as well as enhanced external quantum efficiency (EQE) around 2.21% on LEDs[10] and low-threshold lasing under one and two-photon excitations,[13] these claims have partly been challenged by other groups.[12] Altogether, the literature on tetragonal $CsPb_2Br_5$ and its potential applications in optoelectronics remains very scarce to date, especially with respect to the perovskite $CsPbBr_3$ counterpart. In the meantime, we have also reported the synthesis of $CsPbBr_3$ inks made of NCs capped with short ligands (butylamine and propionic acid). Films prepared from these ligands had a carbon content about 25 times lower than standard NCs.[14] These inks were used as the active material for high-voltage solar cells without any postsynthesis annealing. In the present work, motivated by the aforementioned reports, we investigate the effect of thermal annealing on films of drop-cast short-ligand $CsPbBr_3$ NCs. Indeed, as the observed evolution of NC films upon thermal annealing is linked to the desorption of passivating organic ligands, we observe much more drastic transformations on short-ligand-capped nano-inks than on "standard" long-ligand-capped NCs,[8] with high conversion rate into the tetragonal $CsPb_2Br_5$ phase from 150 °C and significant sintering of the film yielding micrometer-scale grains.

METHODS

Materials. Lead(II) bromide ($PbBr_2$, 99.999% trace metals basis), cesium carbonate (Cs_2CO_3, reagentPlus, 99%), butylamine (BuAm, 99.5%), 2-propanol (iPrOH, anhydrous, 99.5%), propionic acid (PrAc, ≥ 99.5%), and *n*-hexane (HEX 99.5%) were purchased from Sigma-Aldrich. Toluene (TOL, anhy-

Received: April 10, 2017
Revised: May 3, 2017
Published: May 3, 2017

DOI: 10.1021/acs.jpcc.7b03389
J. Phys. Chem. C 2017, 121, 11956−11961

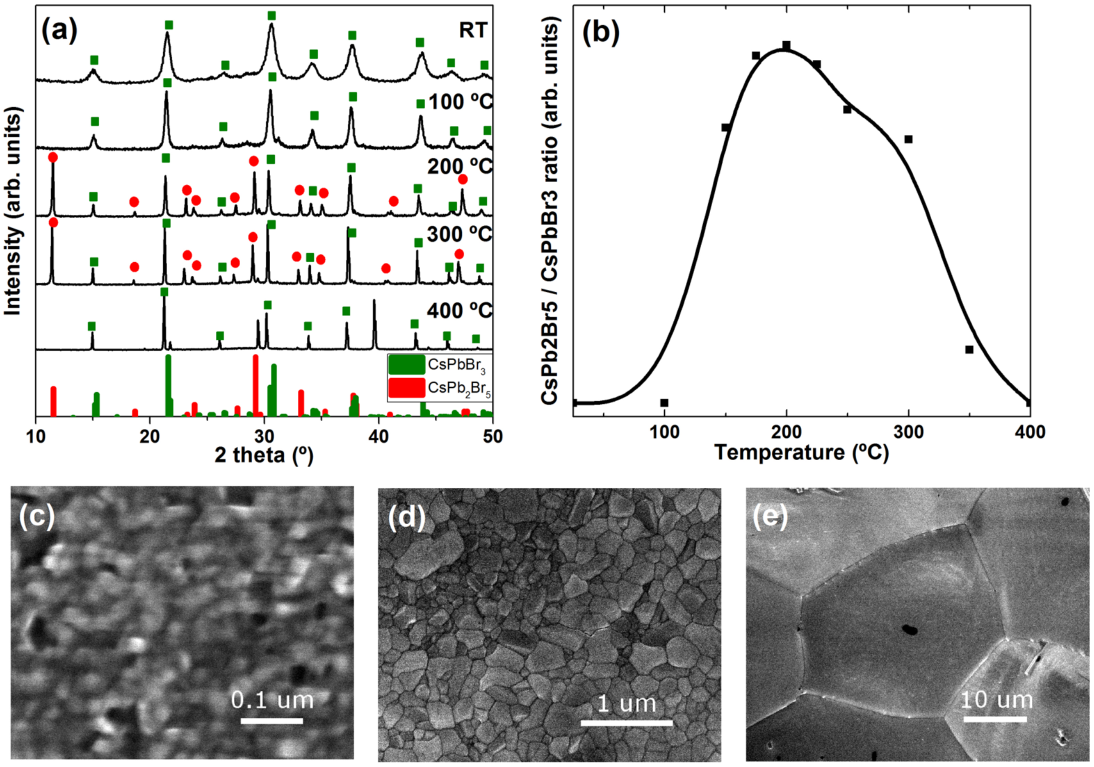

Figure 1. (a) XRD patterns of a film of drop-cast inks upon annealing under nitrogen (see SI for full characterization). (b) Intensity ratio of $CsPb_2Br_5$ and $CsPbBr_3$ main peaks (the solid B-spline line is for easier visualization only). (c−e) HRSEM images of samples at room temperature (c) and after annealing at 200 °C (d) and 400 °C (e).

drous, 99.8%) was purchased from Carlo Erba reagents. All chemicals were used without any further purification.

Synthesis of $CsPbBr_3$ Inks. The $CsPbBr_3$ inks were synthesized as described in our previous report:[14] 2 mL HEX, 1 mL IPrOH, and 5 μL Cs-PrAc (3.6 M Cs^+, Cs_2Co_3 dissolved in pure PrAc at room temperature) were mixed in air at room temperature, forming a clear solution. Swiftly, 200 μL $PbBr_2$ precursor (0.5 M in 1:1:1 PrAc:IPrOH:BuAm) was injected. The solution immediately turned green and it then turned turbid within seconds. The $CsPbBr_3$ NCs were centrifuged for 2 min at 1000 rpm and were then redispersed in toluene.

XRD. High temperature X-ray diffraction analysis (HTXRD) from RT to 400 °C, under inert atmosphere (N_2), was performed using a Rigaku Smartlab system equipped with a 9 kW Cu Kα rotating anode (operating at 40 kV and 150 mA) and an Anton Paar DHS 900 domed hot stage.

SEM. High resolution scanning electron microscopy (HRSEM) analysis was carried out using a JEOL JSM 7500FA scanning electron microscope, equipped with a cold field emission gun (single crystal tungsten ⟨310⟩ emitter). Backscattered electron (BSE) images were acquired at 5 kV beam voltage, using a 2-segment solid state annular detector.

Differential Thermal Analysis/Thermogravimetric-and Mass Spectrometry (DTA/TG MS) Characterization. The DTA/TG investigation (LabsysEvo 1600 − Setaram) was performed from 35 to 400 °C, heating at 5 °C/min in fluent He (20 mL/min). The sample, ∼10 mg, was put into an open alumina crucible. Every minute the autoinjector set at 280 °C (Automation) collects for 10 s, in a loop of 1 mL, the evolved gases from the output of TG; the so collected molecules are injected in the GC (TraceGC Ultra − ThermoFisher): oven and inlet temperatures, respectively, 120 and 280 °C, carrier gas He 1.2 mL/min, split ratio 1:10 and split flow 12 mL/min, column Mega-5 (5%Phenyl/95% Methyl polisiloxane). The GC was coupled to a MS − quadrupole (DSQ I − ThermoFisher) operating in the EI mode (70 eV), ion source at 250 °C, transfer line at 280 °C. The MS scan was performed in the m/z range 29−200.

Photoluminescence Quantum Yield (PLQY) and PL Decay Measurements. Steady-state PL and time-resolved PL decay measurements were carried out on pristine and annealed (at 200 °C) films with an Edinburgh Instruments fluorescence spectrometer (FLS920) which included a xenon lamp with monochromator for steady-state PL excitation and a time-correlated single-photon-counting unit coupled with a pulsed laser diode (excitation wavelength 405 nm) for time-resolved PL decay studies. The stead-state PL spectra on films were collected at the excitation wavelength 400 nm. The PLQY values were obtained on films using a calibrated integrating sphere at the excitation wavelength 400 nm.

Photocurrent Measurements. The interdigitated electrodes were defined by electron-beam lithography followed by thermal evaporation of 4 nm Ti and 50 nm Au. The IV characteristics were performed under vacuum with a probe station (Janis Inc.). To illuminate the films a 473 nm laser diode was used. The time-dependent measurements were carried out by using a chopper to modulate the incoming light. The transient photocurrent was then measured using an oscilloscope (Agilent technologies DSO-X 2014A). The rise time is defined as the time the current needs to rise from 10% to 90% of I_{max} and the fall time as the time the current needs to fall from 90% to 10% of $I_{max,}$ respectively. The photocurrent spectra were recorded by illuminating the films with a ASB-XE-175 xenon light source which was passing through a CM110 1/

DOI: 10.1021/acs.jpcc.7b03389
J. Phys. Chem. C 2017, 121, 11956−11961

8m monochromator to tune the wavelength between 300 nm and 800 nm. The power spectrum of Xe-lamp/monochromator was recorded in the same setup in order to normalize the photocurrent spectra. The power spectrum of the Xe-lamp/monochromator was obtained using a Thorlabs DET10A silicon photodiode.

■ RESULTS AND DISCUSSION

The structural evolution of the film between room temperature and 400 °C in inert atmosphere was monitored by *in situ* X-ray diffraction (XRD) analysis as well as thermal analysis (DTA/TGA) coupled with mass spectrometry (MS) to identify the desorbed species upon annealing. High-resolution scanning electron microscopy (HRSEM) was also used to evaluate the film morphology at different temperatures. Eventually, we used the films as active materials for planar photodetectors. Overall, annealing was found to increase the photocurrent of the film as well as shortening the rise and fall times under intermittent illumination (faster photoresponse). However, this increase in photocurrent and photoresponse was not linear with temperature, suggesting that the chemical transformations occurring in the film (and not only the morphological sintering) play a role in the optoelectronic properties of the material.

The $CsPbBr_3$ nano-inks were synthesized as detailed elsewhere.[14] This synthesis uses short molecular ligands and gives phase-pure $CsPbBr_3$ nanocubes with a typical dimension around 15 nm which are partly welded, forming micrometer-large networks with no well-defined shape. This synthesis has two main advantages over the seminal approach reported by Protesescu et al.[15] when it comes to applications in devices. First, it can be performed on a large scale at room temperature. Second, it yields $CsPbBr_3$ NCs with low organic content due to the short ligands used in the synthesis, such that inter-NC distances are greatly reduced and carriers can move easier across the film. Figure 1a shows the in situ XRD characterization of a film of drop-cast $CsPbBr_3$ nano-inks upon thermal annealing under nitrogen. In the figure only patterns recorded at selected annealing temperatures are shown, while the full set of patterns is reported in Figure S1 of the Supporting Information (SI). The pattern at room temperature matches with the orthorhombic $CsPbBr_3$ reference pattern, with broad peaks due to the nanocrystalline nature of the film. As the film is thermally annealed from room temperature to 400 °C, several observations can be made: in general, peaks become sharper, due to a partial sintering of the NCs into larger grains. Indeed, SEM images show how the original NCs (typical dimension around 15−20 nm) are sintered into grains of ca. 100 nm at 200 °C and tens of microns at 400 °C (see Figure 1c−e). Also, the peaks are progressively shifted toward lower angle values, an indication of the thermal expansion of the unit cell. Another notable evolution of the pattern is the appearance of additional peaks that correspond to tetragonal $CsPb_2Br_5$ phase. This phase is first seen at around 150 °C and fully disappears only at 400 °C, being maximal at 200 °C. The relative intensity of the tetragonal phase main peak (around 11.6°) to the orthorhombic phase main peak (around 30.5°) is plotted in Figure 1b and is indicative of the relative amounts of both phases. The exact amounts are unknown since the reference intensity ratio (RIR) for the tetragonal phase is unknown. However, it is worth noting that the relative conversion to the tetragonal phase at 200 °C is about 30 times higher than for standard NCs.[8,9] This, as will be detailed hereafter, is linked to the shorter and more volatile organic ligands and solvents used here. Eventually, at 400 °C, two additional sharp peaks appear at $2\theta = 29.4°$ and $2\theta = 39.6°$. The former could be linked to the presence of CsBr (ICSD: 98−005−3848) while the latter could not be unambiguously attributed to any known phase.

In order to further elucidate the processes involved in the structural evolutions evidenced by XRD, we performed DTA/TGA of the film in the RT to 400 °C range, coupled with *in situ* gas chromatography and mass spectrometry of the gaseous species that evolved during annealing (Figure 2). The analyses revealed that annealing from RT to 400 °C leads to a moderate weight loss (10.15%) which is linked to the desorption of the solvent and a fraction of the organic ligands. In particular, toluene and propionic acid are unambiguously identified (in Figure 2) by the fragments m/z = 91 and 45, respectively. Butylamine, whose most intense fragment is equal to 30 and overlaps with another fragment from propionic acid (see Figures S3 and S4 in SI for full mass spectra of different organic molecules in the m/z = 28 to m/z = 100 range), was not clearly recognized. However, a release of 2-butene (m/z = 41) occurred in the range 275−350 °C (signals related to m/z = 41 below 275 °C is associated with toluene, see SI) associated with a broad endothermic peak (Figure S2). A second sharper peak was revealed at 356 °C, with no weight loss related, indicating the melting of $PbBr_2$[16] that crystallizes at 310 °C in the cooling curve (Figure S2). By relating these results with the structural evolution observed by in situ XRD, we can detail the following chain of events:

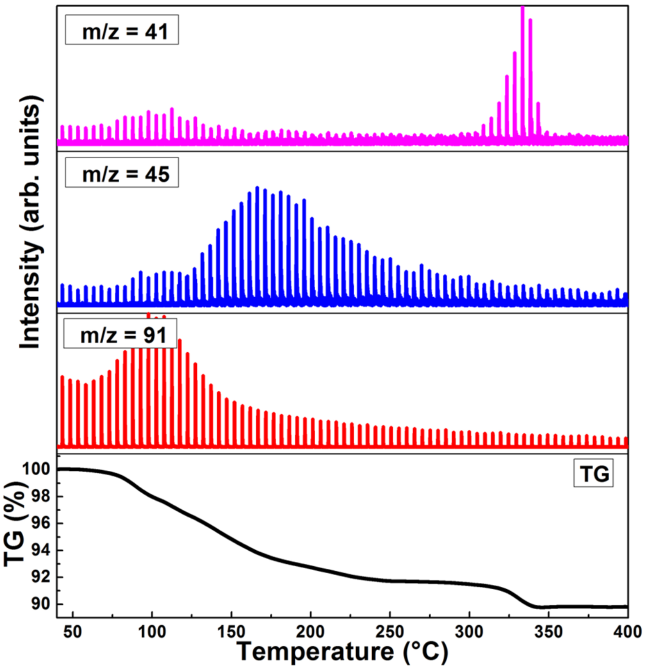

Figure 2. TGA curve and MS traces for toluene (m/z = 91), propionic acid (m/z = 45), and 2-butene (m/z = 41 in the range 275−350 °C) showing the desorption of these small organic molecules. See SI for more details on the identification of the three species.

i. At temperatures around 100 °C, residual solvent (toluene) is evaporated, without significant structural changes on the crystals.

ii. Between 150 and 250 °C, propionic acid is released. This release appears to trigger the phase transformation from $CsPbBr_3$ to $CsPb_2Br_5$, although the exact mechanism remains

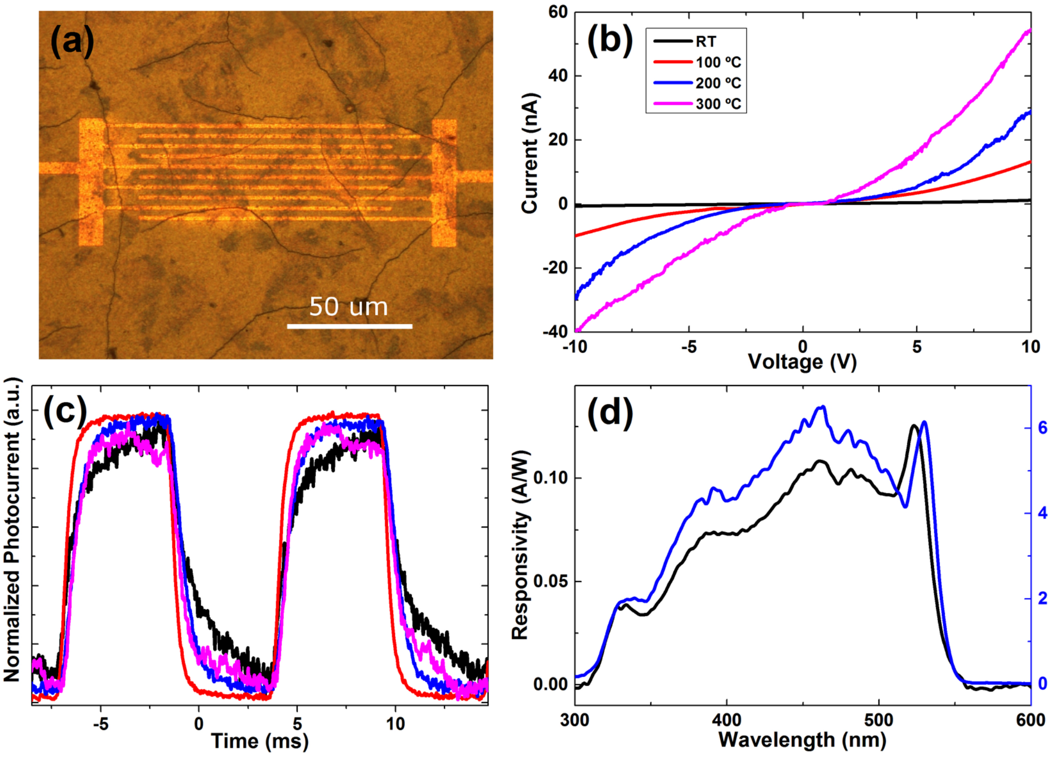

Figure 3. Photocurrent measurements. (a) Optical microscope image of the planar photodetector device. (b) *I*−*V* curves under 8 mW illumination of films annealed at different temperatures. (c) On−Off traces at 92 Hz under 8 mW illumination of films annealed at different temperatures. (d) Photocurrent spectra of pristine film and annealed at 200 °C.

unknown. These data are in line with our previous report on the annealing of films of oleylamine/oleic acid-capped NCs,[8] in which a marginal contribution of the tetragonal $CsPb_2Br_5$ phase appeared only at an annealing temperature of 200 °C, and which is coherent with the higher thermal stability of those longer ligands. In the present case, films annealed at 200 °C show clearly the coexistence of both phases (Figure 1a). Interestingly, confocal fluorescence microscopy images of this film show a spatially nonuniform green emission that does not seem to be correlated with morphology (see Figure S5 in SI). This could suggest a phase segregation between PL-active $CsPbBr_3$ domains and PL-inactive, as demonstrated by others, $CsPb_2Br_5$.[12] The hypothesis of such phase segregation is also supported by contrast differences observed in electron microscopy images using backscattered electrons, more sensitive to material composition (see Figure S5).

iii. At higher temperatures (ca. 325 °C −350 °C) 2-butene is released from the sample, well above its boiling point (−6.6 °C) or that of butylamine (77 °C). It is reasonable to assume that the release of butene derives from strongly bound butylamine, which at high temperature may decompose by losing its amino group through which it is attached to the surface of the NCs, similarly to what has been reported on other short organic molecules that capped inorganic NCs.[17]

As no loss of inorganic material is evidenced by mass spectrometry, we can hypothesize that the transformation from $CsPbBr_3$ to $CsPb_2Br_5$ is accompanied by the formation of CsBr, according to the equation $2CsPbBr_3 \rightarrow CsPb_2Br_5 + CsBr$. In accordance with literature,[11,12,18] this reaction could take place as a two-step process, starting from the decomposition of the initial material ($CsPbBr_3 \rightarrow PbBr_2 + CsBr$), and followed by the reaction of $PbBr_2$ with $CsPbBr_3$ to form the new $CsPb_2Br_5$ phase ($PbBr_2 + CsPbBr_3 \rightarrow CsPb_2Br_5$). Indeed the first step is similar to that already reported upon heating or exposure to moisture on methylammonium-based similar perovskites.[18] The second step has been suggested for the colloidal synthesis of $CsPb_2Br_5$.[11,12] The reverse reaction ($CsPb_2Br_5 \rightarrow PbBr_2 + CsPbBr_3$) takes place above 300 °C, as both XRD (Figure 1) and DTA (Figure S2) suggest. Concerning the presence of CsBr as a side-product of this reaction, it must be noted that its main XRD peak is located at 29.38° (ICSD: 98−005−3848), precisely overlapping the signal of $CsPb_2Br_5$ (secondary peaks from CsBr have significantly less relative intensity and fall outside the range of study). Therefore, it is possible that CsBr cannot be detected by XRD in this case, especially if it forms very small clusters that would give a broad XRD signal.

Eventually, we investigated how these chemical and morphological transformations affected the optoelectronic properties of the film, with a special emphasis on photoconductivity. For this purpose, we deposited a film by drop-casting on top of interdigitated gold electrodes with an electrode spacing of 2 μm on a SiO_2 substrate (see Figure 3a). Without illumination we only observed very low, and mainly nonlinear current that was not sufficiently stable to allow for a detailed discussion. The photocurrent−voltage characteristics after different annealing treatments under monochromatic blue illumination (above band gap) are shown in Figure 3b. The overall photoconductivity was significantly enhanced by the thermal annealing and improved with higher annealing temperatures. The response times (Figure 3c) did not show this continuous trend. Here we found the shortest rise and fall times for the films annealed at 100 °C (1−2 ms). Then for higher annealing temperatures, the response time increased again. Interestingly, the turning point (between 100−200 °C) for the trend change in response time correlates with the temperature (160 °C) for stripping of

DOI: 10.1021/acs.jpcc.7b03389
J. Phys. Chem. C 2017, 121, 11956−11961

propionic acid (see Figure 2), which constitutes the surface passivating ligands. Therefore, the longer response for higher annealing temperature is likely to result from trap states of unpassivated surface regions. This explanation is coherent with the significant drop in photoluminescence quantum yield and faster photoluminescence decay that was observed at 200 °C (see Figure S5 in SI). The photocurrent spectra of pristine and annealed films are shown in Figure 3d, where we observe a well-defined peak around 540 nm that can be related to the band-edge absorption of $CsPbBr_3$ crystals. This peak is slightly red-shifted for the annealed film with respect to the pristine one, which can be rationalized by the increase in grain size due to annealing (this red-shift is also observed in photoluminescence spectra, see Figure S6 in SI). For shorter wavelengths, i.e., excitation above the band gap, we find a broad band with an eventual decrease of photocurrent toward the UV region that is caused by increased scattering of the high energy photoexcited carriers.[19,20]

CONCLUSION

In summary, we demonstrated that annealing films made of $CsPbBr_3$ nano-inks leads to morphological transformations (sintering) and chemical transformations (transformation and vanishing of tetragonal $CsPb_2Br_5$ phase) that we could link to the desorption of different organic species from the film at different temperatures. These transformations affect the photocurrent properties of the film. Mild annealing at 100 °C leads to enhanced photocurrent and faster photoresponse due to the removal of weakly bound organic molecules, and to grain growth without phase transition. Further annealing at 200−300 °C yields maximum conversion to the tetragonal $CsPb_2Br_5$ phase. This transformation is triggered by the further release of propionic acid capping ligands and is accompanied by further sintering. The stripping of the capping ligand also results in the formation of trap states that contribute to a slower photoresponse, albeit higher photocurrent is obtained. Eventually, annealing above 350 °C results in a release of butene coming from strongly bound butylamine ligand after the loss of the amino group. This release triggers the disappearance of the tetragonal $CsPb_2Br_5$ phase. The exact film composition could not be unambiguously determined and no significant photocurrent was recorded on such films. These results shed new light into the possible postsynthesis transformations occurring on annealed inorganic perovskite nanocrystal films and can be used to set guidelines for an optimized use thereof in optoelectronic devices.

ASSOCIATED CONTENT

Ⓢ Supporting Information

The Supporting Information is available free of charge on the ACS Publications website at DOI: 10.1021/acs.jpcc.7b03389.

> Full XRD characterization; DTA curves; mass spectra of different organic molecules; intensity of different m/z fragments as a function of temperature; optical, SEM and PL microscopy images of dual-phase film; PL spectra and PL decay traces of pristine and annealed films at 200 °C (PDF)

AUTHOR INFORMATION

Corresponding Author

*E-mail: liberato.manna@iit.it.

ORCID

Francisco Palazon: 0000-0002-1503-5965
Mirko Prato: 0000-0002-2188-8059
Roman Krahne: 0000-0003-0066-7019
Liberato Manna: 0000-0003-4386-7985

Author Contributions

The manuscript was written through contributions of all authors. All authors have given approval to the final version of the manuscript.

Notes

The authors declare no competing financial interest.

ACKNOWLEDGMENTS

The research leading to these results has received funding from the seventh European Community Framework Programme under Grant Agreement No. 614897 (ERC Consolidator Grant “TRANS-NANO”) and framework Programme for Research and Innovation Horizon 2020 (2014-2020) under the Marie Skłodowska-Curie Grant Agreement COMPASS No. 691185.

REFERENCES

(1) Service, R. F. Cesium Fortifies Next-Generation Solar Cells. *Science* **2016**, *351* (6269), 113−114.

(2) Yantara, N.; Bhaumik, S.; Yan, F.; Sabba, D.; Dewi, H. A.; Mathews, N.; Boix, P. P.; Demir, H. V.; Mhaisalkar, S. Inorganic Halide Perovskites for Efficient Light-Emitting Diodes. *J. Phys. Chem. Lett.* **2015**, *6* (21), 4360−4364.

(3) Ding, J.; Du, S.; Zuo, Z.; Zhao, Y.; Cui, H.; Zhan, X. High Detectivity and Rapid Response in Perovskite $CsPbBr_3$ Single-Crystal Photodetector. *J. Phys. Chem. C* **2017**, *121* (9), 4917−4923.

(4) Swarnkar, A.; Marshall, A. R.; Sanehira, E. M.; Chernomordik, B. D.; Moore, D. T.; Christians, J. A.; Chakrabarti, T.; Luther, J. M. Quantum Dot−Induced Phase Stabilization of a-$CsPbI_3$ Perovskite For High-Efficiency Photovoltaics. *Science* **2016**, *354* (6308), 92−95.

(5) Song, J.; Li, J.; Li, X.; Xu, L.; Dong, Y.; Zeng, H. Quantum Dot Light-Emitting Diodes Based on Inorganic Perovskite Cesium Lead Halides ($CsPbX_3$). *Adv. Mater.* **2015**, *27* (44), 7162−7167.

(6) Ramasamy, P.; Lim, D. H.; Kim, B.; Lee, S. H.; Lee, M. S.; Lee, J. S. All-Inorganic Cesium Lead Halide Perovskite Nanocrystals For Photodetector Applications. *Chem. Commun.* **2016**, *52* (10), 2067−2070.

(7) Zhou, L.; Yu, K.; Yang, F.; Zheng, J.; Zuo, Y.; Li, C.; Cheng, B.; Wang, Q. All-Inorganic Perovskite Quantum Dot/Mesoporous TiO_2 Composite-Based Photodetectors With Enhanced Performance. *Dalton Trans.* **2017**, *46* (6), 1766−1769.

(8) Palazon, F.; Di Stasio, F.; Lauciello, S.; Krahne, R.; Prato, M.; Manna, L. Evolution of $CsPbBr_3$ Nanocrystals Upon Post-Synthesis Annealing Under an Inert Atmosphere. *J. Mater. Chem. C* **2016**, *4* (39), 9179−9182.

(9) Yuan, X.; Hou, X.; Li, J.; Qu, C.; Zhang, W.; Zhao, J.; Li, H. Thermal Degradation of Luminescence in Inorganic Perovskite $CsPbBr_3$ Nanocrystals. *Phys. Chem. Chem. Phys.* **2017**, *19* (13), 8934−8940.

(10) Zhang, X.; Xu, B.; Zhang, J.; Gao, Y.; Zheng, Y.; Wang, K.; Sun, X. W. All-Inorganic Perovskite Nanocrystals for High-Efficiency Light Emitting Diodes: Dual-Phase $CsPbBr_3$-$CsPb_2Br_5$ Composites. *Adv. Funct. Mater.* **2016**, *26* (25), 4595−4600.

(11) Wang, K.-H.; Li, L.; Yao, H.-B.; Qian, H.-S.; Yu, S.-H.; Wu, L. Large-Scale Synthesis of Highly Luminescent Perovskite-Related $CsPb_2Br_5$ Nanoplatelets and Their Fast Anion-Exchange. *Angew. Chem., Int. Ed.* **2016**, *55* (29), 8328.

(12) Li, G.; Wang, H.; Zhu, Z.; Chang, Y.; Zhang, T.; Song, Z.; Jiang, Y. Shape and Phase Evolution From $CsPbBr_3$ Perovskite Nanocubes To Tetragonal $CsPb_2Br_5$ Nanosheets With an Indirect Bandgap. *Chem. Commun.* **2016**, *52* (75), 11296−11299.

(13) Tang, X.; Hu, Z.; Yuan, W.; Hu, W.; Shao, H.; Han, D.; Zheng, J.; Hao, J.; Zang, Z.; Du, J.; Leng, Y.; Fang, L.; Zhou, M. Perovskite $CsPb_2Br_5$ Microplate Laser with Enhanced Stability and Tunable Properties. *Adv. Opt. Mater.* **2017**, *5* (3), 1600788.

(14) Akkerman, Q. A.; Gandini, M.; Di Stasio, F.; Rastogi, P.; Palazon, F.; Bertoni, G.; Ball, J. M.; Prato, M.; Petrozza, A.; Manna, L. Strongly Emissive Perovskite Nanocrystal Inks For High-Voltage Solar Cells. *Nat. Energy* **2016**, *2*, 16194.

(15) Protesescu, L.; Yakunin, S.; Bodnarchuk, M. I.; Krieg, F.; Caputo, R.; Hendon, C. H.; Yang, R. X.; Walsh, A.; Kovalenko, M. V. Nanocrystals of Cesium Lead Halide Perovskites (CsPbX, X = Cl, Br, and I): Novel Optoelectronic Materials Showing Bright Emission with Wide Color Gamut. *Nano Lett.* **2015**, *15* (6), 3692−3696.

(16) Zaitseva, I. Y.; Kovaleva, I. S.; Fedorov, V. A. $HgBr_2$-$CsPbBr_3$ and $CsHgBr_3$-$PbBr_2$ Joins of the $HgBr_2$-$PbBr_2$-CsBr System. *Russ. J. Inorg. Chem.* **2006**, *51* (4), 619−623.

(17) Villa, S.; Riani, P.; Locardi, F.; Canepa, F. Functionalization of Fe_3O_4 NPs by Silanization: Use of Amine (APTES) and Thiol (MPTMS) Silanes and Their Physical Characterization. *Materials* **2016**, *9* (10), 826.

(18) Manser, J. S.; Saidaminov, M. I.; Christians, J. A.; Bakr, O. M.; Kamat, P. V. Making and Breaking of Lead Halide Perovskites. *Acc. Chem. Res.* **2016**, *49* (2), 330−8.

(19) Leatherdale, C. A.; Kagan, C. R.; Morgan, N. Y.; Empedocles, S. A.; Kastner, M. A.; Bawendi, M. G. , Photoconductivity in CdSe Quantum Dot Solids. *Phys. Rev. B: Condens. Matter Mater. Phys.* **2000**, *62* (4), 2669−2680.

(20) Persano, A.; De Giorgi, M.; Fiore, A.; Cingolani, R.; Manna, L.; Cola, A.; Krahne, R. Photoconduction Properties in Aligned Assemblies of Colloidal CdSe/CdS Nanorods. *ACS Nano* **2010**, *4* (3), 1646−52.

DOI: 10.1021/acs.jpcc.7b03389
J. Phys. Chem. C 2017, 121, 11956−11961